Hematite facet confined ferrous ions as high efficient Fenton catalysts to degrade organic contaminants by lowering H_2O_2 decomposition energetic span

Xiaopeng Huang, Xiaojing Hou, Jincai Zhao, Lizhi Zhang*

Key Laboratory of Pesticide & Chemical Biology of Ministry of Education, Institute of Environmental Chemistry, College of Chemistry, Central China Normal University, Wuhan 430079, PR China

ABSTRACT

In this study, we demonstrate that ferrous ions confined on the hematite facets can significantly promote the H_2O_2 decomposition to produce •OH for more efficient organic contaminants degradation than the unconfined counterparts, while hematite nanorods with exposed $\{0\,0\,1\}$ and $\{1\,1\,0\}$ facets exhibit better confining effect than nanoplates with exposed $\{0\,0\,1\}$ facets. Experimental results revealed that the H_2O_2 decomposition efficiency of hematite facet confined ferrous ions was affected by the amount of surface confined ferrous ions, and also governed by the binding mode of ferrous ions on the hematite facets. We interestingly found that the polar $\{1\,1\,0\}$ facets could confine ferrous ions of higher density with a five-coordination binding mode and thus lower the H_2O_2 decomposition energetic span more efficiently than the nonpolar $\{0\,0\,1\}$ facets, which confined ferrous ions with a six-coordination binding mode. The specific surface area normalized •OH formation rate constants were, respectively, 5.50×10^{-3} and $1.04 \times 10^{-2}\,s^{-1}$ for hematite nanoplates and nanorods confined ferrous ions, which were 1.2 and 2.2 times that ($4.75 \times 10^{-3}\,s^{-1}$) of the unconfined counterpart. Moreover, rhodamine B could be efficiently degraded in the presence of hematite ($0.4\,g\,L^{-1}$), Fe^{2+} ($5.0 \times 10^{-5}\,mol\,L^{-1}$) and H_2O_2 ($5.0 \times 10^{-5}\,mol\,L^{-1}$) at pH 4.7, along with 23.6% and 72.5% of H_2O_2 consumption efficiencies for hematite nanoplates and nanorods, respectively. Meanwhile, 6.6% and 11.8% of nitrogen in rhodamine B were converted to NO_3^- in the hematite nanoplates and nanorods confined ferrous ions Fenton systems, respectively. It was found that *N*-deethylation, destruction of chromophores, opening-ring and mineralization occurred during the confined ferrous Fenton rhodamine B oxidation process. This study can deepen our understanding on the enhanced reactivity of ferrous ions bound on the surface of iron oxides, and also shed light on the design of high efficient heterogeneous Fenton catalysts.

1. Introduction

Fenton reaction (Fe^{2+}/H_2O_2) is one of most commonly used advanced oxidation processes because of its high performance, simplicity of technology, and environmental friendliness of the reagents. However, its application is limited by its narrow working pH range (2.5–4) to avoid the precipitation of ferric ions. Heterogeneous Fenton systems with using Fe-containing catalysts like iron oxides, the most abundant minerals in the Earth's crust, could widen the working pH range [1–7]. Among the iron oxides, hematite is the most thermodynamically stable form. Unfortunately, hematite cannot efficiently catalyze the H_2O_2 decomposition to produce hydroxyl radical at pH >4. It is therefore of great importance to improve the H_2O_2 decomposition efficiency of hematite.

Iron oxide crystal surfaces are chemically reactive to water and ions with facet selectivity. For example, when hematite is subjected to oxygen-limited aquatic environments in acidic conditions, its $\{hk0\}$ surfaces can be reductively dissolved to produce Fe^{2+} adsorbed on the $\{0\,0\,1\}$ surfaces. These adsorbed Fe^{2+} would then reduce Fe^{3+} in the hematite, yielding an iron redox cycle where no net reduction occurs [8]. Therefore, ferrous ions ubiquitously coexist with hematite in natural aquatic environments. Normally, the fundamental reactions between Fe^{2+} ions and iron oxide surfaces can be described with the interfacial electron transfer (IET) model, which involves the generation of amorphous ferric oxides like $Fe^{II}OFe^{III}OH$ and $Fe^{II}OFe^{III}$ via confining ferrous ions on the hematite surfaces [9]. It is well known that ferrous ions bound (confined)

on iron oxides exhibit much higher reactivity than the dissolved ferrous ions. For instance, Fe(II) adsorbed on iron (hydr)oxide surfaces or surface coatings could induce the reduction of substituted nitrobenzenes, but the dissolved ferrous ions were inactive [10], while the nitroaromatic compounds could be reduced efficiently by mineral-bound Fe(II) species [11]. Unfortunately, the intrinsic reasons for the high reactivity of ferrous ions confined on iron oxides are still unclear.

In this study, we demonstrate that ferrous ions confined on the different hematite facets can significantly promote the H_2O_2 decomposition to produce hydroxyl radical for the organic contaminants degradation than the unconfined counterpart, while hematite nanorods with exposed {0 0 1} and {1 1 0} facets exhibit better confining effect than nanoplates with exposed {0 0 1} facets. The interesting facet dependent ferrous ions confinement phenomenon and their catalytic property are investigated in detail.

2. Experiments section

2.1. Chemicals and materials

Ferric chloride hexahydrate, sodium acetate, sodium oleate, oleic acid, ammonium chloride, hydrogen peroxide (H_2O_2, 30%), sodium hydroxide, acetic acid, ferrous sulfate heptahydrate, hydrochloric acid, potassium acid phthalate, benzoic acid, iso-propanol, potassium chloride, and Al_2O_3 powders (particles size, 50 μm) were analytical reagents and purchased from Sinopharm Chemical Reagent Co. Ltd., China. P-hydroxyphenylacetic acid (PHPA) and horseradish peroxidase (POD, specific activity of 100 units m^{-1}) were purchased from Aladdin Chemistry Co. Ltd., China. Rhodamine B (RhB, >99%) and Amberlite IR-120 ion exchange resin were obtained from Alfa-Aesar, USA. Nafion PFSA polymer dispersions (D520, 5%) was obtained from DuPont, USA. Deionized water was used throughout the experiments apart from the total organic carbon and ion chromatography measurements. All the chemicals were used as received without purification.

2.2. Sample preparation

Different hematite architectures were synthesized with previously reported hydrothermal and solvothermal methods [12,13]. For the synthesis of hematite nanoplates (HNPs), 1.09 g of FeCl$_3$·6H$_2$O (4.0 mmol) was dissolved in 40.0 mL of ethanol under magnetic stirring, followed with the addition of 2.8 mL of deionized water and then 3.2 g of sodium acetate. The mixture was stirred for 2 h at room temperature until the complete formation of homogeneous solution. The solution was sealed in a 100 mL Teflon-lined stainless steel autoclave and heated in an oven at 180 °C for 12 h. The precipitation was collected and washed thoroughly with deionized water and ethanol, and finally dried in a desiccator at 40 °C for 12 h. As for the synthesis of hematite nanorods, 1.35 g of FeCl$_3$·6H$_2$O was added to 77 mL of 0.16 mol L^{-1} NH$_4$Cl aqueous solution and then stirred for 2 h. The resulting homogeneous solution was transferred into 100 mL Teflon-lined stainless steel autoclave, and heated at 120 °C for 12 h. The resulting FeOOH precipitation was collected, rinsed with water and ethanol and finally dried at 40 °C for 12 h. The FeOOH sample was calcined at 520 °C for 2 h with a heating rate of 10 °C min^{-1} in air to obtain the hematite nanorods for use.

2.3. Characterizations

The powder of the catalyst were identified by powder X-ray diffraction measurements (XRD, D/Max-IIIA X-ray diffractometer, Cu Kα radiation, λ = 0.15418 nm) for crystalline conditions. Then, the samples were characterized by DXR Raman Microscope with a 532 nm laser excitation source (∼2 mW) through a 50× objective lens. The morphologies of the samples were obtained by scanning electron microscopy (SEM), transmission electron microscopy (TEM, JEOL-2010, 200 kV). High-resolution transmission electron microscopy (HRTEM, JEOL, JSM-2010) were used to confirm the phase lattice and determine the dominant facets of the samples. The data of BET (Brunauer–Emmett–Teller) surface areas were obtained from nitrogen adsorption isotherms with a Micromeritics Tristar3000 instrument.

2.4. Electrochemical tests

The hematite modified glass carbon (GC) electrode was prepared using a bare GC electrode with a diameter 3 mm. Typically, the GC electrode was polished with emery paper and Al_2O_3 powders. The polished electrode was cleaned with iso-propanol and water in an ultrasonic bath for 10 min, respectively. The hematite slurry containing 4 mg of hematite was prepared with a dilute Nafion solution composed of 100 μL of Nafion (5%) and 5 mL of iso-propanol. Then 5 μL of the above hematite slurry was coated on the polished GC electrode by using a microsyringe. The resulting hematite modified GC electrode was dried with the infrared lamp for use. Electrochemical measurements were carried out in a standard three-electrode cell consisting of a working electrode with hematite modified electrode, a counter electrode with platinum spiral, and a saturated calomel electrode (SCE). The open-circuit potentials (E_{OCP}) were obtained with a potentiostat (CHI660D, China) at a scan rate 50 mV s^{-1}. The 25 mL electrochemical cell was filled with a solution of 1.0×10^{-2} mol L^{-1} KCl and 1.0×10^{-3} mol L^{-1} FeSO$_4$ for the measurement. The pH of the solution (pH = 0, 1, 2, 3, 4, and 5) was adjusted by HCl and NaOH solutions.

2.5. H_2O_2 concentration measurement

The concentration of hydrogen peroxide was analyzed using a modified p-hydroxyphenylacetic acid (POHPAA) emission method [14]. In the POHPAA method, the fluorescent dimmer (FD) was formed via the reaction of hydroperoxides with POHPAA, catalyzed by horseradish peroxidase. The FD has a strong fluorescent emission at 409 nm when excited at 315 nm. Fluorescence spectra of the sample solution were measured with the fluorescence spectrophotometer (FL1008M018, Cary, USA). To prepare the fluorescence reagent, 1 mg of POD and 2.7 mg of POHPAA were successively added in the 10 mL of 8.2 g L^{-1} potassium acid phthalate aqueous solution. 50 μL of fluorescence reagent was added to 2 mL of sample solution, followed with the addition of 1 mL of 0.1 mol L^{-1} NaOH solution after 10 min for the subsequent fluorescence measurements.

2.6. Quantification of •OH, TOF and energetic span (δE)

A widely used method to calculate the time-dependent •OH concentration is to introduce •OH sink and a chemical •OH probe [15]. The rate of hydroxyl radicals concentration change with respect to time is described by the following equation:

$$\frac{d[\bullet OH]}{dt} = V_{\bullet OH} - k_{\bullet OH,P}[\bullet OH][P] - \sum k_{\bullet OH,S}[\bullet OH][S] \qquad (1)$$

where V is the formation rates of hydroxyl radical, P and S are representative of the probe and other scavengers, respectively.

In the case of high probe concentration ([P]/[H_2O_2] > 1000), the scavenging effect of H_2O and other compounds can be safely ruled out (Eq. (2)). So Eq. (1) can be simplified to Eq. (3), and $[P]_T$ is the

average concentration of the chemical probe.

$$V_s = \sum k_{\bullet OH,S}[\bullet OH][S]$$
$$= k_{\bullet OH,H_2O}[\bullet OH][H_2O] + k_{\bullet OH,other}[\bullet OH][other] = 0 \qquad (2)$$

$$V_{\bullet OH} = \frac{-d[P]}{dt} = k_{\bullet OH,P}[P]_T \qquad (3)$$

Simultaneously, we measured the H_2O_2 concentration during reaction. With using Eq. (4), we plotted the •OH generation rates *vs* the H_2O_2 concentration. The slope of the fitting line was regarded as the rate constant of •OH generation, which was the normalized rate constants $k_{\bullet OH}'$ of hematite confined ferrous ions Fenton system.

$$V_{\bullet OH} = k_{\bullet OH,P}[P] = k_{\bullet OH}'[SSA][H_2O_2] \qquad (4)$$

The dispersion of active ferrous ions confined on facets (D_{Fe}) was calculated with the surface area (A), the site density of ferrous ions (Q), the moles of total iron (n_{Fe}), and the Avogadro constant (N_A) according to the following equation:

$$D_{Fe} = \frac{A \times Q}{n_{Fe} \times N_A} \qquad (5)$$

The turnover frequency (TOF) as the turnover number of hydrogen peroxide into •OH per second on one active site, can be calculated with $V_{\bullet OH}$, D_{Fe} and the moles of hematite ($n_{Fe_2O_3}$) according to the following equation:

$$TOF = \frac{V_{\bullet OH}}{D_{Fe} \times n_{Fe_2O_3}} \qquad (6)$$

We can calculate the average •OH generation rate constants and TOF of the homogenous Fenton catalyst. Therefore, the initial TOF of homogeneous Fenton system was calculated with the initial formation rates of hydroxyl radical ($V_{\bullet OH,0}$) and the concentration of ferrous ions ([Fe(II)]) according to the following equation:

$$TOF_0 = \frac{V_{\bullet OH,0}}{[Fe(II)]} \qquad (7)$$

According to the energetic span (δE) model, δE can be obtained from the TOF via Eq. (8), where R is the gas constant (8.314 J K^{-1} mol^{-1}), k_b is the Boltzmann constant (1.38×10^{-23} J K^{-1}), h is the Planck constant (6.626×10^{-34} J s), T is 293.15 K as room temperature.

$$\delta E = RT \left(\ln \frac{k_b T}{h} - \ln TOF \right) \qquad (8)$$

In this study, benzoic acid (BA) was used as the probe molecule. The concentration of benzoic acid was determined by high performance liquid chromatography (HPLC, Shimadzu SB-C18 reverse phase column, 10 μL injection volume). Typically, samples were collected at regular intervals using a 2 mL syringe and filtered immediately through a 0.22 μm nylon syringe filter. The isocratic elution was composed of 30% acetonitrile and 70% water (pH = 2). The flow rate is 1 mL min^{-1} and the detection wavelength is 270 nm.

2.7. Fenton degradation experiments

All the degradation experiments were carried out in 100 mL conical flask in dark with constant stirring at room temperature. The initial concentrations of contaminants (rhodamine *B*, methylene blue, and methyl violet) were 5 mg L^{-1}. Each 50 mL reaction solution with desired concentrations of organic contaminants was prepared with deionized water. Hydrogen peroxide, hematite and ferrous ions were added in sequence to the organic contaminant solutions. The pH value was changed to 4.7 after ferrous ions added into the rhodamine B solution. The initial pH values of control experiments were adjusted to 4.7 with adding 2.0 mol L^{-1} chloric

acid solution. Samples were taken out at pre-arranged time intervals for the subsequent measurement. The concentration of organic contaminants was measured by a UV–vis 2550 spectrophotometer (Shimadzu, Japan).

2.8. Mineralization test

The mineralization processes were monitored with using total organic carbon (TOC) and ion chromatography. Ultrapure water was used to minimize the effect of impurities on the experimental results. TOC was measured with a TOC-V$_{CPH}$ analyzer (Shimadzu, Japan) after filtration through 0.22 μm filter. The concentrations of ions were detected with a Dionex ICS-900 ion chromatograph (Thermo, USA).

3. Results and discussion

3.1. Characterization of the samples

The powder X-ray diffraction pattern (Fig. S1a in the SM) and Raman spectra (Fig. S2a in the SM) analyses revealed that both of the samples were pure α-Fe$_2$O$_3$ with a rhombohedral hexagonal phase. Scanning electron microscopy (SEM), transmission electron microscopy (TEM), and high-resolution transmission electron microscopy (HRTEM) were then used to characterize the morphology and structure of the resulting samples. SEM and TEM characterizations revealed that the two α-Fe$_2$O$_3$ architectures were of well-defined shape (Fig. 1 and Fig. S2 in the SM). The hexagonal HNPs had a narrow size distribution with an average width of 79.3 nm and a mean thickness of 15.5 nm (Fig. 1a–b and Fig. S2a–b in the SM). The distinguishable lattice fringe of 0.25 nm in the HRTEM image was consistent with {1 1 0}, {−2 1 0}, {−1 2 0} planes of HNPs, as confirmed by the FFT pattern (Fig. 1c–d). This revealed that these nanoplates were exposed with {0 0 1} and {1 0 2} planes of ca. 81.6% and 18.4% proportions in HNPs, and thus the hematite nanoplates were mainly exposed with {0 0 1} facet. SEM and TEM images demonstrated that the length, width, and height of HNRs were about 453.8, 72.6, and 72.6 nm, respectively (Fig. 1e–f and Fig. S2c–d in the SM). The lattice fringes of 0.25 nm was consistent with {1 1 0}, {−1 2 0}, {−2 1 0} planes of α-Fe$_2$O$_3$ according to the HRTEM image and the corresponding FFT patterns (Fig. 1g–h). SEM and TEM images analyses revealed that HNRs were of about 45.8% {0 0 1}, 45.8% {1 1 0}, 4.2% {1 2 0} and 4.2% {2 1 0} facets, suggesting that the hematite nanorods were mainly exposed with {0 0 1} and {1 1 0} facets. Table 1 summarizes the detail physicochemical properties of two α-Fe$_2$O$_3$ nanoarchitectures.

3.2. The interaction of hematite facets with ferrous ions

The interaction of different α-Fe$_2$O$_3$ facets with Fe^{2+} ions was first investigated by comparing the Fe^{2+} ions adsorption on the two α-Fe$_2$O$_3$ nanoarchitectures at pH 4.7 (the initial pH value after the addition of ferrous ions). The adsorption capacities were obtained from the adsorption kinetic curves (Fig. 2). As revealed by Table 1, HNPs had much higher apparent maximum ferrous ions adsorption capacity (Q_{max} = 4.35 mg g^{-1}) than HNRs (Q_{max} = 2.26 mg g^{-1}). As the total site densities of Fe^{2+} species were positively correlated with the specific surface areas of α-Fe$_2$O$_3$ nanoarchitectures, the surface area normalized total site densities were calculated to be 2.24 and 7.28 #Fe/nm^2 for HNPs and HNRs, respectively. Regarding that hematite nanorods and nanoplates were mainly exposed with {1 1 0} and/or {0 0 1} facets, we subsequently estimated the iron species confined on the individual facet, which were 2.74 and 13.15 #Fe/nm^2 for the {0 0 1} and {1 1 0} facets of hematite, respectively. Therefore, ferrous ions could be adsorbed on the {1 1 0} facet with much higher density than the {0 0 1} facet of hematite. The different
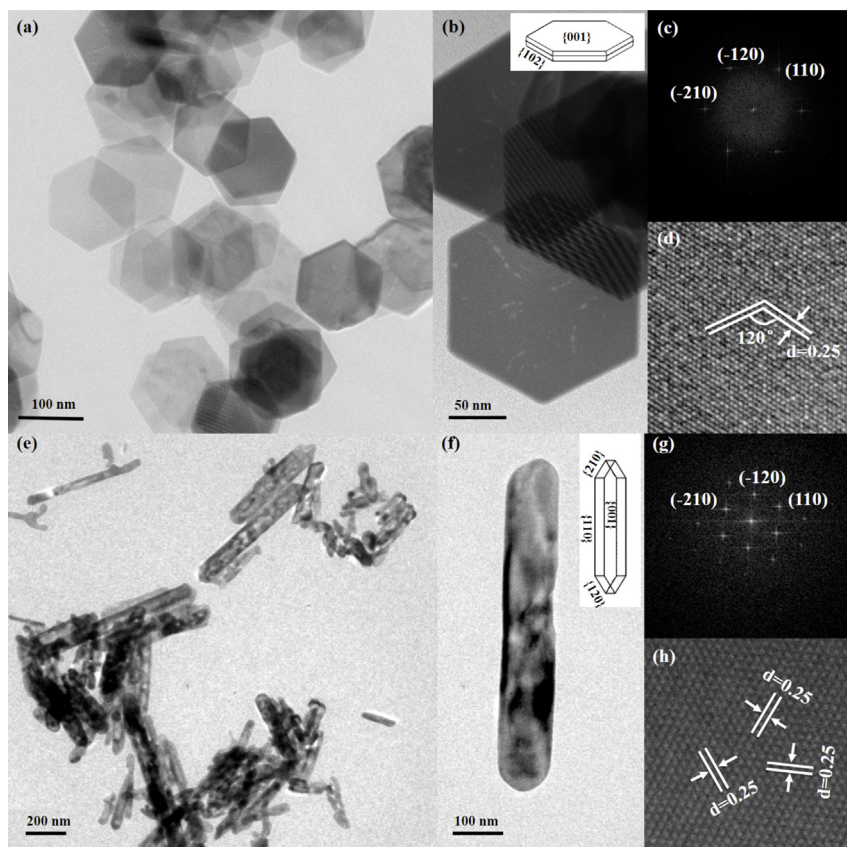
Fig. 1. Representative morphology and crystalline structure of HNPs and HNRs. (a) TEM image, (b) a single nanoplate and schematic shape of a plate (Inset), (c) FFT pattern, and (d) high-resolution TEM image of HNPs; (e) TEM image, (f) a single nanorod and schematic shape of a rod (Inset), (g) FFT pattern, and (h) high-resolution TEM image of HNRs.

properties of adsorption kinetics might be explained via the interaction between surface charge and ferrous ions. The adsorption of ferrous ions on the α-Fe$_2$O$_3$ surfaces was further investigated with electrochemical methods [8,16–19]. We measured the open-circuit potentials (E_{OCP}) of α-Fe$_2$O$_3$ architectures in the potassium chloride aqueous solution in the absence or presence of ferrous ions at different pH values of 0, 1, 2, 3, 4, and 5. The approximately linear pH dependent curves with predominantly negative slopes were consistent with the accumulation of positive surface charge with decreasing pH (Fig. 3). As expected, the HNRs with {1 1 0} facet exposure possessed a more negative slope in the absence of ferrous ions because of their more density charge accumulation sites than the HNPs. Moreover, the open-circuit potential curve of HNRs was more sensitive to the addition of ferrous ions, confirming that

more density charge accumulation sites favored the ferrous ions confinement on the facets of hematite.

3.3. Hematite facet confined ferrous ions Fenton systems

To distinguish from the traditional Fenton (Fe^{2+}/H$_2$O$_2$) system, we called the combination of ferrous ions confined on the facets of hematite and H$_2$O$_2$ as the ferrous ions confined Fenton system. We subsequently measured the concentration of dissolved ferrous ions in different Fenton systems as the function of time with the 1,10-phenanthroline colorimetrical method. As expected, the dissolved ferrous ions were quickly decreased within 30 min in all the Fenton systems. Obviously, hematite enhanced the dissolved ferrous ions consumption because ferrous ions would be

Table 1
Physicochemical properties of HNPs and HNRs.

Sample	Length[a] [nm]	Width [nm]	Height [nm]	SSA[b] [m²/g]	Q$_{max}$[c] [mg/g]	Site density [#Fe/nm²]	Exposed Facets[d]	Surface area ratio [100%]	k[e] [min⁻¹]	k/Q$_{max}$ [g/(mg min)]
HNPs	–	79.3	15.5	20.9	4.35	2.24	{0 0 1} {1 0 2} or {0 1 2}	81.6 18.4	0.0955	0.0219
HNRs	453.8	72.6	72.6	2.6	1.76	7.28	{0 0 1} {1 1 0} {1 2 0} or {2 1 0}	45.8 45.8 8.4	0.1436	0.0816

[a] The morphological characteristics were calculated by using SEM and TEM.
[b] The specific surface area (SSA) was determined by N$_2$ adsorption-desorption of hematite nanostructures.
[c] Q_{max} = maximum adsorption capacity obtained by the adsorption kinetics curves. Site density = ($Q_{max} \times 10^{-3} \times 6.02 \times 10^{23}$)/($56 \times$ SSA $\times 10^{18}$).
[d] The exposed facets were determined by using TEM and HRTEM.
[e] k was the H$_2$O$_2$ decomposition rate calculated by the decomposition kinetics curves.
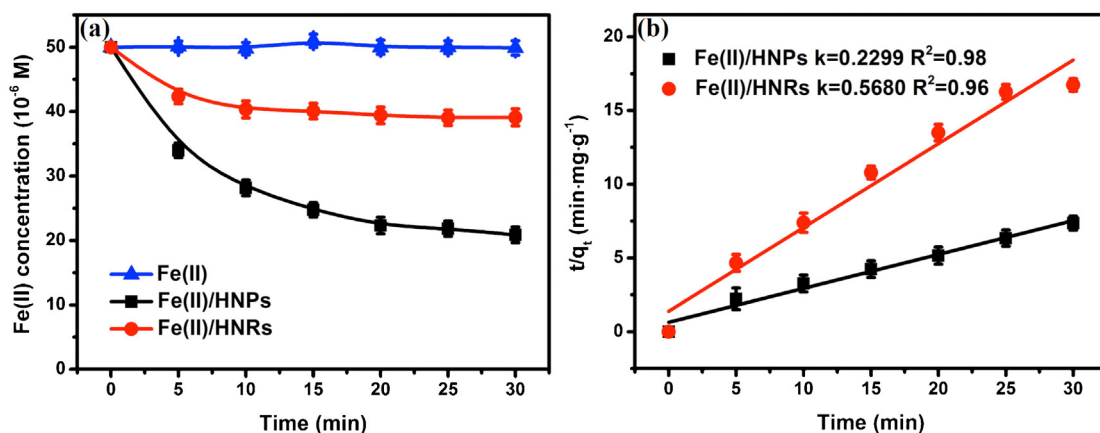
Fig. 2. (a) Comparison the adsorption of Fe(II) ions on the as-prepared α-Fe$_2$O$_3$ architectures; (b) Adsorption kinetics curves of Fe(II) ions. The initial concentration of Fe(II) was 5.0×10^{-5} mol L^{-1}; the dosage of α-Fe$_2$O$_3$ architectures was 0.4 g L^{-1}; the initial pH was 4.7.
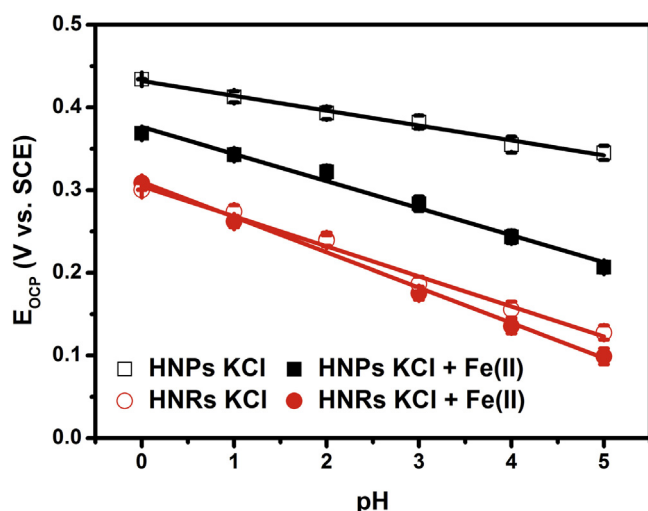

Fig. 3. The pH dependent open-circuit potentials of HNPs and HNRs with respect to saturated calomel electrode (SCE) in 1.0×10^{-2} mol L^{-1} KCl solution in the absence and presence of 1.0×10^{-3} mol L^{-1} Fe^{2+}. The scan rate was 50 mV s^{-1}.

absorbed and subsequently oxidized by H$_2$O$_2$ on the nanoarchitectures. The equilibrium concentration of dissolved ferrous ions was 9.88×10^{-6} mol L^{-1} for the traditional Fenton system, accounting for about 20% of initial ferrous ions added. Nevertheless, the equilibrium concentrations of dissolved ferrous ions in the HNPs and

HNRs confined ferrous ions Fenton systems were, respectively as low as 7.78×10^{-6} and 2.60×10^{-6} mol L^{-1}, which were about 16% and 5% of the initial value (Fig. 4a). The surface confined ferrous ions of two nanoarchitectures were then calculated with the HCl extraction technique [7,9]. Within 30 min, the surface confined ferrous ions were found to be 2.50×10^{-6} mol g^{-1} (about 2% of the initial ferrous ions added) for HNPs mainly exposed with {0 0 1} facet, and 5.80×10^{-7} mol g^{-1} (about 0.5% of the initial ferrous ions added) for HNRs mainly exposed with {0 0 1} and {1 1 0} facets. Thus, the surface area normalized confined Fe(II) were 5.96×10^{-6} and 1.12×10^{-5} mol m^{-2} for HNPs and HNRs, respectively (Fig. 4b). These results confirmed the higher density of ferrous ions confined on the {1 1 0} facet of hematite.

The reactivity of ferrous ions confined on the different hematite architectures were then evaluated with the catalytic H$_2$O$_2$ decomposition at pH 4.7. The decomposition of H$_2$O$_2$ in the confined Fenton systems was found to obey pseudo-first-kinetic equation (Fig. 5). The apparent H$_2$O$_2$ decomposition rate constants (k) were, respectively calculated to be 0.0955 and 0.1436 min^{-1} for the ferrous ions confined on HNPs and HNRs, revealing that ferrous ions confined on the facets of HNRs were more efficient for the H$_2$O$_2$ decomposition than the counterparts on the facets of HNPs. To check the influence of different ferrous ions adsorption amounts of α-Fe$_2$O$_3$ architectures on their H$_2$O$_2$ decomposition efficiency, we normalized their apparent decomposition rate constants with their maximum ferrous ions adsorption capacity (Q_{max}). The k/Q_{max} values were calculated to be 0.0219 and 0.0816 g mg^{-1} min^{-1} for the ferrous ions confined on HNPs and HNRs, respectively. The
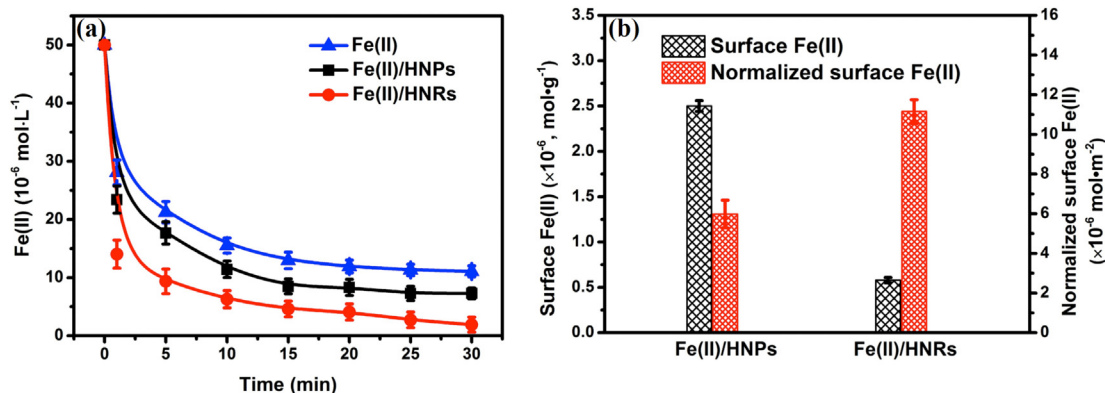

Fig. 4. (a) Fe(II) concentration in aqueous solutions as a function of time in the presence of α-Fe$_2$O$_3$ architectures and H$_2$O$_2$; (b) The surface and normalized surface Fe(II) concentration in the presence of α-Fe$_2$O$_3$ architectures, Fe(II), and H$_2$O$_2$. The initial concentrations of Fe(II) and H$_2$O$_2$ were 5.0×10^{-5} mol L^{-1} and 5.0×10^{-5} mol L^{-1}, respectively; the dosage of α-Fe$_2$O$_3$ architectures was 0.4 g L^{-1}; the initial pH was 4.7.
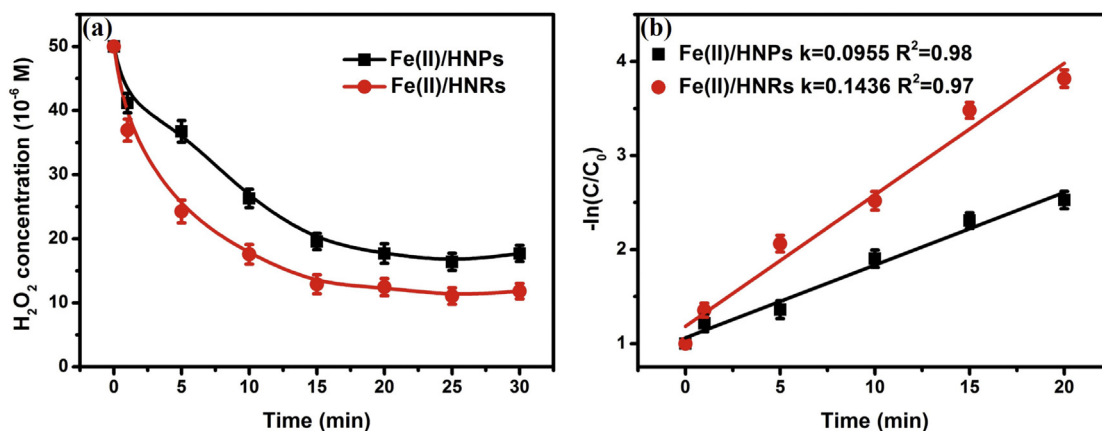
Fig. 5. (a) Comparison the decomposition of H_2O_2 in the presence of α-Fe_2O_3 architectures, Fe(II), and H_2O_2; (b) Decomposition kinetics curves of H_2O_2. The initial concentrations of Fe(II) and H_2O_2 were 5.0×10^{-5} mol L^{-1} and 5.0×10^{-5} mol L^{-1}, respectively; the dosage of α-Fe_2O_3 architectures was 0.4 g L^{-1}; the initial pH was 4.7.

normalized H_2O_2 decomposition rate constant of ferrous ions confined HNRs was still about 3.7 times that of ferrous ions confined HNPs, suggesting that the H_2O_2 decomposition efficiency of α-Fe_2O_3 architectures was not only affected by the amount of surface confined ferrous ions, but also by other factors.

It is highly possible that the binding mode of ferrous ions on the facets of hematite is vital for the H_2O_2 decomposition. To confirm this opinion, we first compared the ferrous ions adsorption on the two facets of hematite theoretically. As for the hematite crystal structure, each Fe atom is surrounded by six O atoms, whereas each O atom is bound to four Fe atoms in a typical hematite crystal unit (Fig. S3a in the SM). A hematite crystal has a rhombohedrally centered hexagonal structure with a closed-packed lattice, in which two-thirds of the octahedral sites are occupied by Fe^{3+} ions. Each octahedron shares edges with three neighboring octahedral in the same plane and one face with another octahedron in an adjacent plane (Fig. S3b in the SM). The confinement of foreign atoms or molecules on the hematite facets is related to its intrinsic crystal structure. For instance, foreign atoms or molecules (e.g., ferrous ions) can intercalate into the interlayer, the tunnels, and the holes in the crystal structure [13]. As seen from the hematite structure along [0 0 1] and [1 1 0], there is no interlayer space or tunnel in the crystal structure (Fig. S4 in the SM). Upon careful observation of the hematite surface structure, the holes are observed in the first octahedral layer, and thus able to confine ferrous ions on the {0 0 1} and {1 1 0} surface. Upon the side view of hematite {0 0 1}, the unreacted {0 0 1} facet has both Fe- and O-terminations (Fig. S5a–b in the SM). Moreover, the {0 0 1} facet is relatively inert to the protonation and deprotonation reactions for the charge accumulation owing to its nonpolar surface characteristic [20,21]. When the {0 0 1} facet is subjected to the ferrous ions aqueous solution, the co-existing structural domains would be modified via the adsorption of ferrous ions by the holes of hematite, resulting in six-coordinated ferrous ions adsorbed on the surface (Fig. 6). This six-coordination binding mode was validated by the nucleation of homoepitaxial hematite-like islands on {0 0 1} surface [22,23].
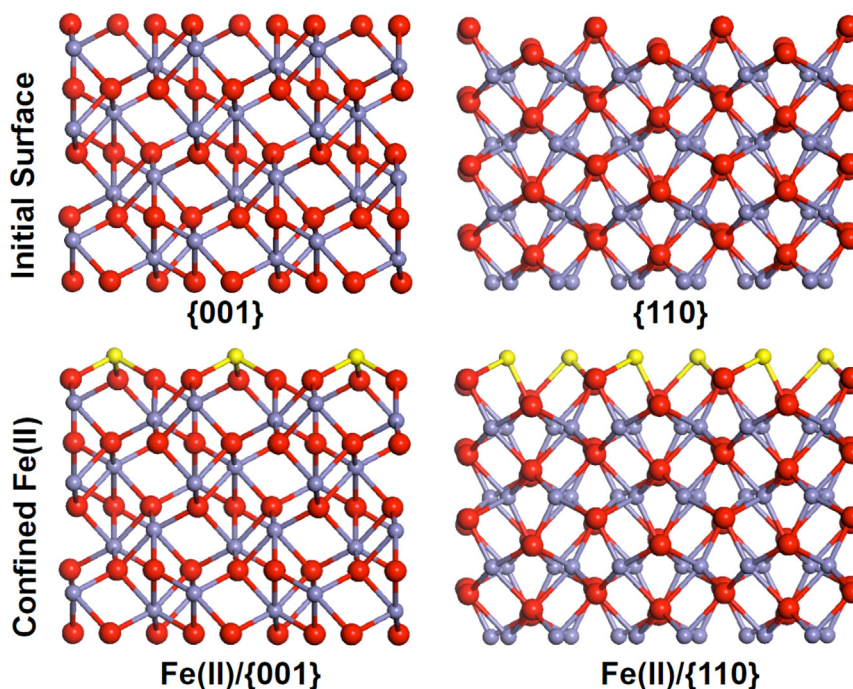

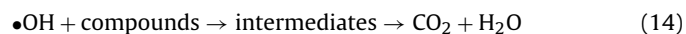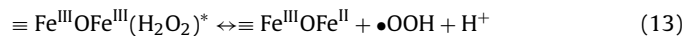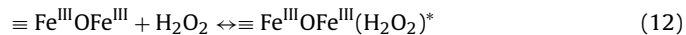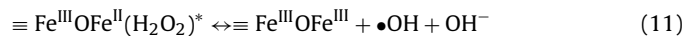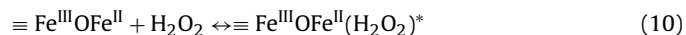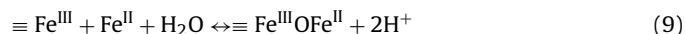**Fig. 6.** Schematic models to illustrate the confinement of Fe(II) on the {0 0 1} and {1 1 0} surfaces of hematite. Oxygen atoms are red spheres, bulk iron atoms are blue spheres and confined ferrous iron atoms on the surfaces are yellow spheres.

Obviously, the confined ferrous ions of hematite-like islands on the {0 0 1} facet contributes to the charge accumulation of {0 0 1} facet in this study. As for the hematite {1 1 0} surface, there is only one plausible surface termination with the octahedral coordination of the surface Fe layer (Fig. 6). Thus, the resulting unreacted surface of {1 1 0} displays a unique ridge-and-valley topography of five-coordinated Fe (Fe_{5c}) surface sites (Fig. 6) [23]. The existence of surface Fe_{5c} sites endows the {1 1 0} facet with a typical polar surface [20,24]. Therefore, the {1 1 0} facet relatively favors the protonation and deprotonation reactions for the charge accumulation. When the {1 1 0} facet is subjected to the ferrous ions aqueous solution, the surface Fe_{5c} sites would be modified via the adsorption of ferrous ions by the holes of hematite to confine ferrous ions on the surface with a five-coordination mode. This five-coordination binding mode was verified by the layer-by-layer growth/dissolution on the {1 1 0} surface [8,23]. We therefore conclude that the five-coordination binding mode of ferrous ions confined on the {1 1 0} facet can benefit the charge accumulation, and also more efficiently decompose H_2O_2 than the six-coordination binding mode. Similar phenomenon was observed for anatase TiO_2 with exposed {0 0 1} and {1 0 1} facets during heterogeneous processes. For instance, owing to the abundant undercoordinated Ti atoms on the surface, both anatase TiO_2 with exposed {0 0 1} and {1 0 1} facets exhibited enhanced performance [25–29]. Whereas, experimental and surface energy calculation results revealed that {0 0 1} faceted anatase TiO_2 with 100% five-coordinated Ti atoms were more reactive than {1 0 1} faceted anatase TiO_2 with 50% five-coordinated Ti atoms and 50% six-coordinated Ti atoms during the heterogeneous water adsorption and methanol adsorption processes [25–29].

The hematite facets confined ferrous ions would produce strong Lewis acid sites on the surface (Eq. (9)), which would promote various chemophysical processes such as complexation and ions adsorption. As a Lewis base, H_2O_2 has a stronger affinity to the surface confined ferrous ions than H_2O. Therefore, the hematite facets confined ferrous ions would be attacked by H_2O_2 to form the complex state $\equiv Fe^{III}OFe^{II}(H_2O_2)^*$ (Eq. (10)). Because of the strong reducibility of confined ferrous ions, electrons would transfer from the confined ferrous ions to H_2O_2 with generating surface ferric ($\equiv Fe^{III}OFe^{III}$) and $\bullet OH$ (Eq. (11)). Meanwhile, the generated $\equiv Fe^{III}OFe^{III}$ could be partially reduced by H_2O_2 to realize the Fe(III)/Fe(II) cycle (Eqs. (12–13)). The generated $\bullet OH$ would oxidize organic contaminants finally (Eq. (14)) (Scheme 1).

$$\equiv Fe^{III} + Fe^{II} + H_2O \leftrightarrow \equiv Fe^{III}OFe^{II} + 2H^+ \tag{9}$$

$$\equiv Fe^{III}OFe^{II} + H_2O_2 \leftrightarrow \equiv Fe^{III}OFe^{II}(H_2O_2)^* \tag{10}$$

$$\equiv Fe^{III}OFe^{II}(H_2O_2)^* \leftrightarrow \equiv Fe^{III}OFe^{III} + \bullet OH + OH^- \tag{11}$$

$$\equiv Fe^{III}OFe^{III} + H_2O_2 \leftrightarrow \equiv Fe^{III}OFe^{III}(H_2O_2)^* \tag{12}$$

$$\equiv Fe^{III}OFe^{III}(H_2O_2)^* \leftrightarrow \equiv Fe^{III}OFe^{II} + \bullet OOH + H^+ \tag{13}$$

$$\bullet OH + compounds \rightarrow intermediates \rightarrow CO_2 + H_2O \tag{14}$$

The influence of different hematite facet confined ferrous ions on the H_2O_2 decomposition was further investigated thermodynamically by comparing their energetic spans for the H_2O_2
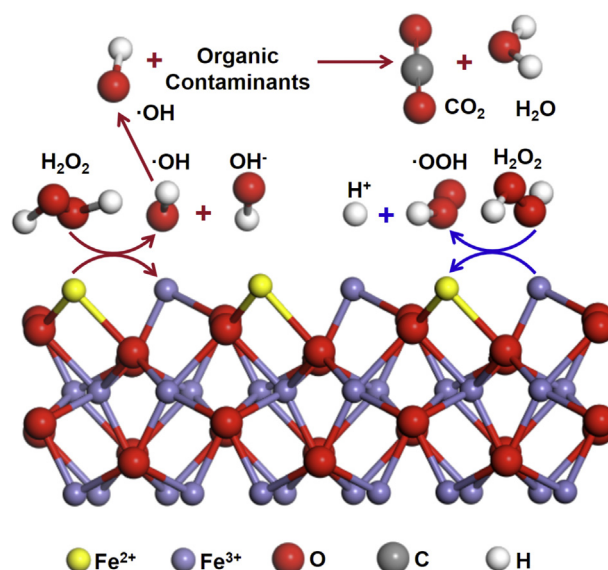
Scheme 1. Schematic illustrations of hematite facets confined ferrous ions as Fenton catalysts to degrade organic contaminants.

decomposition. According to the energetic span (δE) model [30–33], δE can be obtained from the turnover frequency (TOF), which can be calculated by using the chemical probe method. The TOF values of HNPs and HNRs confined ferrous ions, as defined by the turn number of hydrogen peroxide into $\bullet OH$ per second on one active site, were calculated 1.80×10^{-2} and $6.52 \times 10^{-1}\,s^{-1}$, respectively (Table 2). These values were much higher than that ($1.53 \times 10^{-2}\,s^{-1}$) of the unconfined ferrous ions of traditional Fenton system. Meanwhile, the δE of HNPs and HNRs confined ferrous ions were, respectively 11.14 and 9.05 kcal mol^{-1}. Thus, the δE of HNRs confined ferrous ions was significantly lower than those of unconfined (11.23 kcal mol^{-1}) and HNPs confined counterparts, which might be arisen from the five-coordination binding mode of ferrous ions confined on the {1 1 0} facet of HNRs. Besides the dissolved ferrous ions, we interestingly found that the hematite facet confined ferrous ions were much more efficient than other iron-containing materials such as goethite (α-FeOOH), ferrihyrite ($Fe_5HO_8 \bullet 4H_2O$), hematite (α-Fe_2O_3) for the H_2O_2 decomposition to produce active species (Table 2) [15,34,35].

In the Fenton system, the active species were probably hydroxyl radical ($\bullet OH$) and high-valent iron-oxo complex such as ferryl ion (FeO^{2+}) [36–41]. Thus, the active species trapping experiments were employed to identify the major active species generated in the confined Fenton system with iso-propanol as the $\bullet OH$ scavenger and ethanol as the scavenger for both $\bullet OH$ and high-valent iron-oxo complex. The same scavenging effect of excessive iso-propanol and ethanol suggested that hydroxyl radical was the major oxidative species in the confined Fenton system (Fig. S6 in the SM), which was further confirmed by the benzoic acid probe method [42]. Benzoic acid was then used to quantify hydroxyl radical generated

Table 2
Comparison of $\bullet OH$ formation rates for different iron-containing materials.

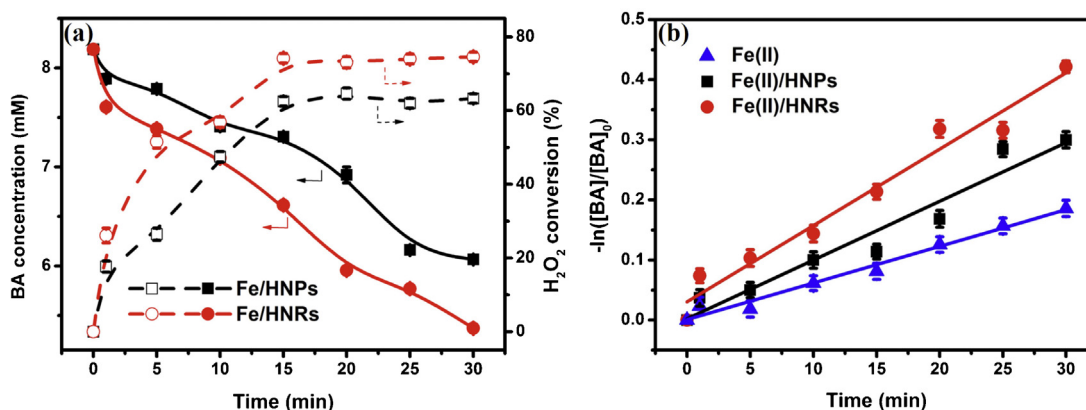| Material	TOF [s^{-1}]	$k_{\bullet OH}$ [s^{-1}]	$k_{\bullet OH}'$ [g s^{-1} m^{-2}]	δE [kcal mol^{-1}]	Ref.
α-Fe_2O_3	–	4.00×10^{-7}	8×10^{-9}	–	[34]
α-FeOOH	–	4.25×10^{-5}	10^{-7}	–	[34]
$Fe_5HO_8 \cdot 4H_2O$	–	2.00×10^{-5}	10^{-7}	–	[34]
Fe(II)	1.53×10^{-2}	4.75×10^{-3}	–	11.23	This study
Fe(II)/HNPs	1.80×10^{-2}	5.50×10^{-3}	2.63×10^{-4}	11.14	
Fe(II)/HNRs	6.52×10^{-1}	1.04×10^{-2}	4.00×10^{-3}	9.05	
Fe(II)	–	4.40×10^{-3}	–	–	[35]
Fe(II+a)	1.25×10^{-3}	2.5×10^{-4}	–	13.62	[15]

Fig. 7. (a) Transformation of BA (solid line) and H_2O_2 (dashed line) over confined ferrous catalysts; (b) Oxidation of BA over hematite in the presence of Fe(II) and H_2O_2. The initial concentrations of BA, Fe(II) and H_2O_2 were 8.189×10^{-3} mol L^{-1}, 5.0×10^{-5} mol L^{-1} and 5.0×10^{-5} mol L^{-1}, respectively; the dosage of α-Fe_2O_3 architectures was 0.4 g L^{-1}; the initial pH was 4.7.

Table 3
The rate constants of degradation of benzoic acid (k_p) and the apparent formation rates of hydroxyl radicals ($V_{\bullet OH}$).

Sample	k_p [s^{-1}]	$V_{\bullet OH}$ [M s^{-1}]
Fe(II)	1.02×10^{-4}	7.64×10^{-7}
Fe(II)/HNPs	1.63×10^{-4}	1.17×10^{-6}
Fe(II)/HNRs	2.12×10^{-4}	1.44×10^{-6}

in the ferrous ions confined Fenton system (Fig. 7 and Fig. S7 in the SM). Benzoic acid was partially oxidized accompanying with a ~70% conversion of H_2O_2 in the first 15 min, while little further decomposition of H_2O_2 in the later 15 min (Fig. 7a). The oxidation rates of benzoic acid (k_p) were obtained from the kinetic curves (Fig. 7b). The k_p (1.63×10^{-4} s^{-1} for HNPs and 2.12×10^{-4} s^{-1} for HNRs) of ferrous ions confined Fenton system were much higher than that (1.02×10^{-4} s^{-1}) of the unconfined counterpart (Table 3). Then, the generation rates of hydroxyl radical ($V_{\bullet OH}$) were evaluated from k_p and the average concentration of benzoic acid, which were 7.64×10^{-7}, 1.17×10^{-6}, and 1.44×10^{-6} M s^{-1} for the unconfined ferrous ions, the HNPs confined ferrous ions, and the HNRs confined ferrous ions, respectively (Table 3). We plotted the generation rates of hydroxyl radical versus the H_2O_2 concentration (Fig. 8a) and obtained the apparent rate constants of $\bullet$OH formation ($k_{\bullet OH}$). The $k_{\bullet OH}$ of confined Fenton system (5.50×10^{-3} s^{-1} for HNPs and 1.04×10^{-2} s^{-1} for HNRs) were 1.2 and 2.2 times that (4.75×10^{-3} s^{-1}) of the unconfined counterpart. Meanwhile, the specific surface area normalized $k_{\bullet OH}$ ($k_{\bullet OH}'$) was calculated to be 2.63×10^{-4} and 4.00×10^{-3} g s^{-1} m^{-2} for the HNPs and HNRs confined ferrous ions, respectively (Fig. 8b), confirming that ferrous

ions confined on the {1 1 0} facet of hematite with undercoordination mode could more efficiently catalyze the H_2O_2 decomposition than the {0 0 1} counterpart.

3.4. Organic pollutants degradation in confined Fenton systems

The confined Fenton systems were then employed to oxidize various organic compounds including rhodamine B (RhB), methylene blue, and methyl violet, and then compared with the traditional Fenton system at the initial pH of 4.7. We found that all these organic contaminants could be efficiently degraded in the Fenton and confined Fenton systems and their degradation curves within 30 min obeyed the pseudo-first-kinetic equation. Regarding the xanthene cationic dye nature and hardly biodegradable characteristic of RhB, we therefore chose RhB as a model contaminant to investigate the Fenton oxidation performance of different facet confined ferrous ions in detail. First, we investigated the RhB degradation in the hematite facet confined ferrous ions Fenton systems in the presence of 2.0×10^{-5}, 5.0×10^{-5} and 8.0×10^{-5} mol L^{-1} of H_2O_2 and found the RhB degradation rate first increased along with increasing the H_2O_2 concentration and then kept steady (Fig. S8 in the SM). The RhB degradation rate in case of 5.0×10^{-5} mol L^{-1} H_2O_2 was close to that of 8.0×10^{-5} mol L^{-1} H_2O_2. Thus, 5.0×10^{-5} mol L^{-1} was chosen as the optimal concentration of H_2O_2 in this study. For comparison, a control experiment at pH 4.7 was conducted in the presence of H_2O_2 and hematite (Fig. S9 in the SM), or Fe^{2+} and hematite (Fig. S10 in the SM). The RhB degradation was not observed in the presence of H_2O_2 and hematite because α-Fe_2O_3 is not able to activate H_2O_2
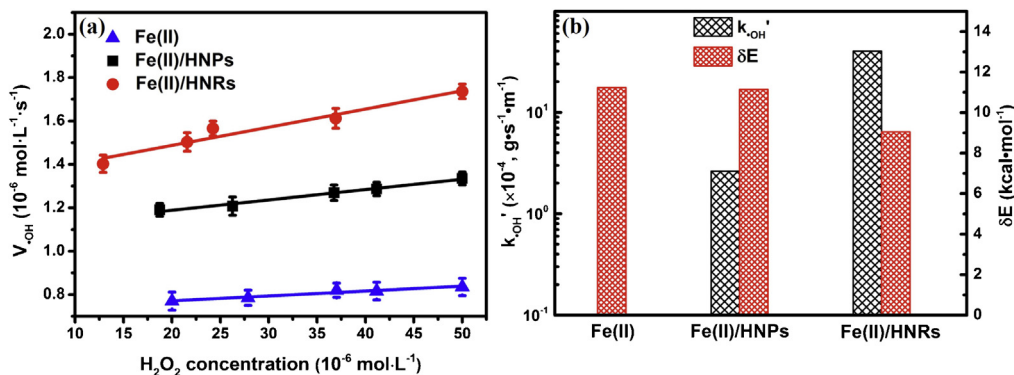

Fig. 8. (a) Formation rates of $\bullet$OH as a function of H_2O_2 concentration in the different Fenton systems; (b) Normalized formation rate constants of $\bullet$OH and energetic spans (δE) in the different Fenton systems.
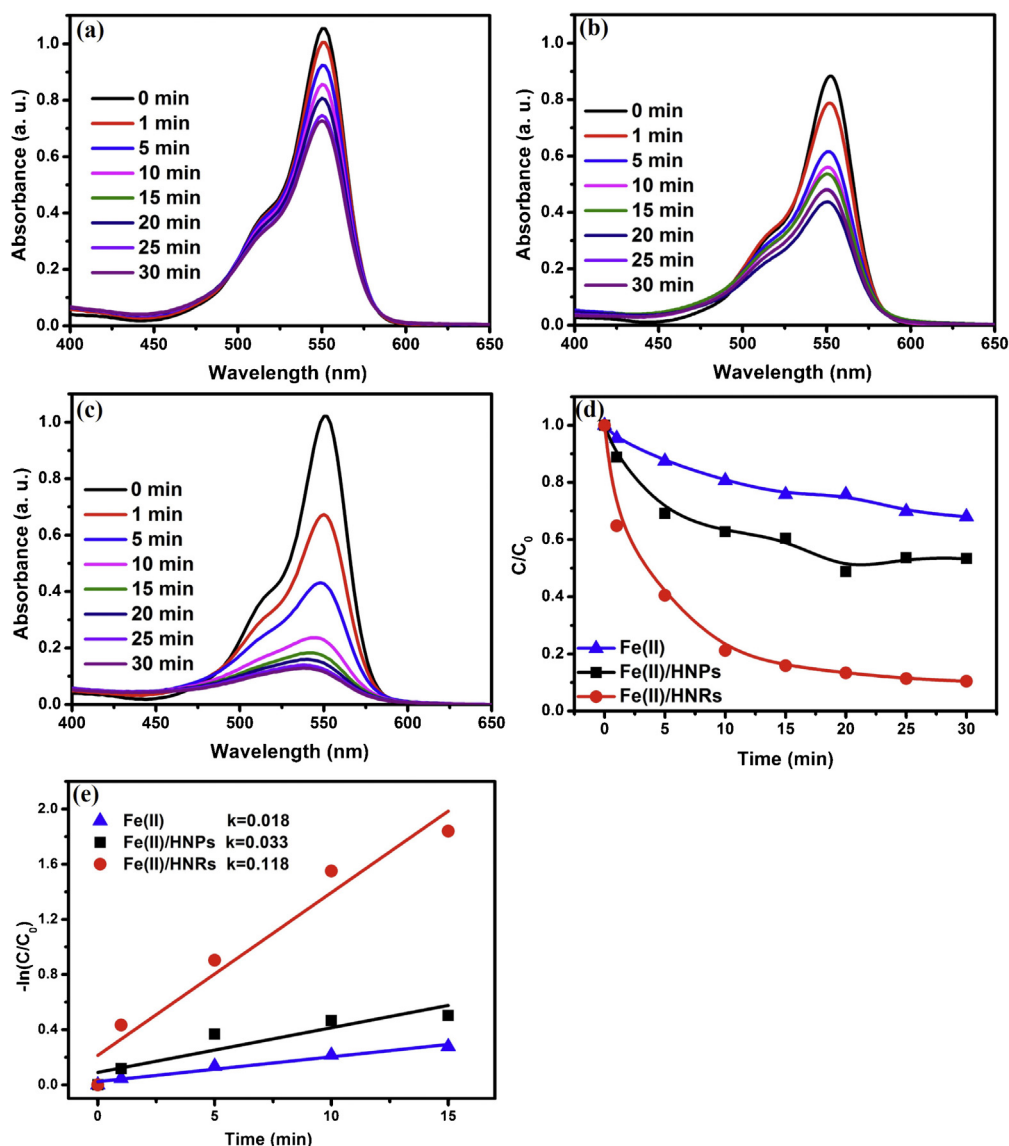
Fig. 9. UV–vis spectral changes of RhB aqueous solutions as a function of time in the presence of α-Fe$_2$O$_3$, H$_2$O$_2$, and Fe(II). (a) Fe(II) and H$_2$O$_2$; (b) Fe(II)/HNPs and H$_2$O$_2$; (c) Fe(II)/HNRs and H$_2$O$_2$; (d) The degradation curves of RhB; (e) The degradation kinetics curves of RhB. Linear regression equation in initial time. Pseudo-first order kinetic model $\ln(c/c_0) = -kt$ and the plot represents apparent reaction rate constants of the system. The initial concentrations of RhB, Fe(II) and H$_2$O$_2$ were 5 mg L^{-1}, 5.0×10^{-5} mol L^{-1} and 5.0×10^{-5} mol L^{-1}, respectively; the dosage of α-Fe$_2$O$_3$ architectures was 0.4 g L^{-1}; the initial pH was 4.7.

significantly. Meanwhile, the combination of Fe^{2+} and hematite could not induce the RhB degradation in the absence of H$_2$O$_2$. Interestingly, RhB could be efficiently degraded in the hematite facet confined ferrous Fenton systems (Fig. 9), consistent with the •OH measurement results. It was found that the absorbance of RhB decreased with the absorption peak shifting to lower wavelength, especially for the {1 1 0} facet confined ferrous ions Fenton system. The apparent rate constants (3.29×10^{-2} min^{-1} for Fe(II)/HNPs, 1.18×10^{-1} min^{-1} for Fe(II)/HNRs) of RhB degradation in the facet confined ferrous ions Fenton systems were 1.8 and 6.5 times that (1.8×10^{-2} min^{-1}) of the unconfined counterpart. We interestingly found that the surface area normalized RhB degradation rate constant (1.13×10^{-1} min^{-1} L m^{-2}) of HNRs confined ferrous ions Fenton system was even about 29 times that (3.95×10^{-3} min^{-1} L m^{-2}) of HNPs counterpart (Table 4), further confirming that ferrous ions confined on the {1 1 0} facet of hematite with undercoordination mode could more efficiently catalyze the H$_2$O$_2$ decomposition to oxidize organic pollutants than the {0 0 1} counterpart.

The reusability of hematite nanorods was then studied. After 5 cycles of reaction, hematite nanorods could still exhibit remarkable activity, although slightly lower than that of the freshly prepared sample (Fig. S11 in the SM), confirming their reusability. Moreover, we monitored the dissolved iron concentration change during the RhB degradation and found that dissolved iron concentration first decreased and then kept steady (1.9×10^{-5} mol L^{-1} for Fe(II)/HNPs, 1.6×10^{-5} mol L^{-1} for Fe(II)/HNRs) in the confined ferrous ions Fenton systems (Fig. S12 in the SM), suggesting that the hematite facet confinement could prevent the generation of iron sludge during wastewater treatment.

The mineralization of RhB in the confined ferrous ions Fenton systems was also investigated. The TOC removal percentages were 13.0% and 49.4% for the HNPs and HNRs confined ferrous ions Fenton systems, respectively (Table 5). The H$_2$O$_2$ consumption efficiency, namely the TOC reduction per unit of H$_2$O$_2$ consumption, was also calculated for the confined ferrous ions Fenton oxidation of RhB (Fig. S13 in the SM). The H$_2$O$_2$ consumption efficiencies were found to be 55.0% and 68.1% for the Fe(II)/HNPs and Fe(II)/HNRs,

Table 4
Degradation of various organic compounds in Fenton and ferrous ions confined Fenton systems.

Entry	RhB		Methylene blue		Methyl violet	
	k [a] [min^{-1}]	k_s [b] [min^{-1} L m^{-2}]	k [min^{-1}]	k_s [min^{-1} L m^{-2}]	k [min^{-1}]	k_s [min^{-1} L m^{-2}]
Fe(II)	1.80×10^{-2}	–	4.45×10^{-2}	–	7.33×10^{-3}	–
Fe(II)/HNPs	3.29×10^{-2}	3.95×10^{-3}	4.94×10^{-2}	5.91×10^{-3}	1.15×10^{-2}	1.38×10^{-3}
Fe(II)/HNRs	1.18×10^{-1}	1.13×10^{-1}	5.27×10^{-2}	5.07×10^{-2}	1.05×10^{-2}	1.01×10^{-2}

[a] The apparent reaction rate constants (k) of contaminants degradation were calculated based on a pseudo-first-order kinetic model.
[b] Rate constants (k_s) were normalized to specific surface area, as calculated via $k_s = k/$(catalyst concentration $\times$ SSA).

Table 5
Change of TOC and NO$_3^-$ concentrations before and after reactions in the traditional Fenton and confined ferrous Fenton system.

entry	Initial TOC [ppm]	Final TOC [ppm]	TOC removal [a] [%]	Initial NO$_3^-$ [ppm]	Final NO$_3^-$ [ppm]	NO$_3^-$ increase [ppm]
Fe(II)	4.346	3.895	10.4	0.1390	0.1421	0.0031
Fe(II)/HNPs	4.382	3.812	13.0	0.1644	0.2406	0.0762
Fe(II)/HNRs	4.515	2.331	49.4	0.1644	0.3010	0.1366

TOC removal (%) was calculated based on the following equation: TOC removal = $(TOC_0 - TOC_t)/TOC_0 \times 100\%$, where TOC_0 was initial TOC of RhB and TOC_t is final TOC of RhB.

respectively. Therefore, the H_2O_2 consumption efficiencies were 23.6% and 72.5% for the HNPs and HNRs confined ferrous ions Fenton systems, respectively. We interestingly found that the H_2O_2 consumption efficiencies of hematite facet confined ferrous ions (e. g. Fe(II)/HNRs) were much higher than those of other iron-containing materials (Table S1 in the SM) [43,44]. Meanwhile, ion chromatography analysis revealed the formation of NO_3^- species. 0.1366 ppm of NO_3^- was generated during the RhB degradation in the HNRs confined ferrous ions Fenton system, which was about 1.8 times that (0.0762 ppm) in the HNPs counterpart (Table 5). The theoretical concentration of NO_3^- was 1.16 ppm if all the nitrogen of RhB were converted into NO_3^- species. Therefore, 6.6% and 11.8% of nitrogen in RhB were converted to NO_3^- in the HNPs and HNRs confined ferrous ions Fenton systems, respectively.

Gas chromatograph-mass spectroscopy was then used to investigate the degradation intermediates to propose the possible RhB oxidation pathway in the confined ferrous ions Fenton system. The RhB degradation intermediates, including dimethyl phthalate, 2-(2,5-dihydroxyphenyl) acetic acid, phthalic acid, 2,6-dihydroxybenzoic acid, 2-hydroxybenzoic acid, malonic acid, 2-hydroxypropanoic acid, 2-oxopropanoic acid, 2-hydroxyacetic acid, acetic acid and N-methylethanamine, were detected (Fig. S14 in the SM), confirming that RhB was degraded via the oxidation pathway in the confined ferrous ions Fenton system. Generally, N-deethylation and destruction of chromophores are competitive in the first step of RhB degradation. During the RhB degradation, the maximum absorption of 554 nm decreased gradually along with a blue shift (Fig. 9), suggesting that N-deethylation and destruction of chromophores happened simultaneously. After N-deethylation and destruction of chromophores, opening-ring would occur and then be followed with mineralization. On the basis of the above results, we propose a possible RhB degradation pathway in the confined ferrous ions Fenton system at pH 4.7 (Fig. S15 in the SM).

4. Conclusions

In summary, we have demonstrated that the H_2O_2 decomposition efficiency of hematite facet confined ferrous ions is not only affected by the amount of surface confined ferrous ions, but also governed by the binding mode of ferrous ions on the hematite facets. This is because the hematite {1 1 0} facet can confine ferrous ions with higher density, and also produce surface ferrous ions with undercoordination mode to favor the H_2O_2 decomposition and thus account for the enhanced reactivity of ferrous ions bound on iron oxides. The specific surface area normalized •OH formation rate constants were, respectively 5.50×10^{-3} and 1.04×10^{-2} s^{-1} for

hematite nanoplates and nanorods confined ferrous ions, which were 1.2 and 2.2 times that (4.75×10^{-3} s^{-1}) of the unconfined counterpart. Rhodamine B could be efficiently degraded in the presence of hematite (0.4 g L^{-1}), Fe^{2+} (5.0×10^{-5} mol L^{-1}) and H_2O_2 (5.0×10^{-5} mol L^{-1}) at pH 4.7, along with 23.6% and 72.5% of H_2O_2 consumption efficiencies for hematite nanoplates and nanorods, respectively. Meanwhile, 6.6% and 11.8% of nitrogen in RhB were converted to NO_3^- in the hematite nanoplates and nanorods confined ferrous ions Fenton systems, respectively. It was found that N-deethylation, destruction of chromophores, opening-ring and mineralization occurred during the confined ferrous Fenton rhodamine B oxidation process. Regarding the coexistence of Fe^{2+} ions with hematite ubiquitously in natural aquatic environments, the understanding of intrinsic reasons for the enhanced reactivity of ferrous ions bound on iron oxides will have three important environmental implications. The first one is to transfer the organic contaminants to low or no-toxic products with ferrous ions confined on the facets of iron containing minerals. The second one is to give us a better understanding of the internal relationship between the iron redox cycling process and organic pollutants degradation in the aspect of Environmental Science. The third one is to design high efficient heterogeneous Fenton catalysts with surface confinement effect, as revealed in this study.

Appendix A. Supplementary data

Supplementary material related to this article can be found, in the online version, at http://dx.doi.org/10.1016/j.apcatb.2015.06.061

References

[1] X.J. Yang, X.M. Xu, Y.F. Han, J. Am. Chem. Soc. 135 (2013) 16058–16061.
[2] S.S. Lin, M.D. Gurol, Environ. Sci. Technol. 32 (1998) 1417–1423.
[3] L.W. Chen, J. Ma, X.C. Li, J. Zhang, J.Y. Fang, Y.H. Guan, P.C. Xie, Environ. Sci. Technol. 45 (2011) 3925–3930.
[4] A.L.T. Pham, C. Lee, F.M. Doyle, D.L. Sedlak, Environ. Sci. Technol. 43 (2009) 8930–8935.

[5] K. Hanna, T. Kone, G. Medjahdi, Catal. Commun. 9 (2008) 955–959.
[6] H.H. Huang, M.C. Lu, J.N. Chen, Water Res. 35 (2001) 2291–2299.
[7] C.K. Duesterberg, S.E. Mylon, T.D. Waite, Environ. Sci. Technol. 42 (2008) 8522–8527.
[8] S.V. Yanina, K.M. Rosso, Science 320 (2008) 218–221.
[9] B.H. Jeon, B.A. Dempsey, W.D. Burgos, Environ. Sci. Technol. 37 (2003) 3309–3315.
[10] J. Klausen, S.P. Troeber, S.B. Haderlein, R.P. Schwarzenbach, Environ. Sci. Technol. 29 (1995) 2396–2404.
[11] T.B. Hofstetter, R.P. Schwarzenbach, S.B. Haderlein, Environ. Sci. Technol. 37 (2003) 519–528.
[12] L. Chen, X. Yang, J. Chen, J. Liu, H. Wu, H. Zhan, C. Liang, M. Wu, Inorg. Chem. 49 (2010) 8412–8418.
[13] C. Wu, P. Yin, X. Zhou, C. Ouyang, Y. Xie, J. Phys. Chem. B 110 (2006) 17806–17812.
[14] A.L. Lazrus, G.L. Kok, J.A. Lind, S.N. Gitlin, B.G. Heikes, R.E. Shetter, Anal. Chem. 58 (1986) 594–597.
[15] M.E. Lindsey, M.A. Tarr, Chemosphere 41 (2000) 409–417.
[16] F. Gaboriaud, J.J. Ehrhardt, Geochim. Cosmochim. Acta 67 (2003) 967–983.
[17] P. Venema, T. Hiemstra, P.G. Weidler, W.H. van Riemsdijk, J. Colloid Interface Sci. 198 (1998) 282–295.
[18] F.B. Li, L. Tao, C.H. Feng, X.Z. Li, K.W. Sun, Environ. Sci. Technol. 43 (2009) 3656–3661.
[19] G.V. Nano, T.J. Strathmann, J. Colloid Interface Sci. 297 (2006) 443–454.
[20] J.M. Vohs, Chem. Rev. 113 (2012) 4136–4163.
[21] C.M. Eggleston, A.G. Stack, K.M. Rosso, S.R. Higgins, A.M. Bice, S.W. Boese, R.D. Pribyl, J.J. Nichols, Geochim. Cosmochim. Acta 67 (2003) 985–1000.
[22] K.S. Tanwar, S.C. Petitto, S.K. Ghose, P.J. Eng, T.P. Trainor, Geochim. Cosmochim. Acta 73 (2009) 4346–4365.
[23] J.G. Catalano, P. Fenter, C. Park, Z. Zhang, K.M. Rosso, Geochim. Cosmochim. Acta 74 (2010) 1498–1512.
[24] J.R. Rustad, E. Wasserman, A.R. Felmy, Surf. Sci. 424 (1999) 28–35.
[25] M. Lazzeri, A. Vittadini, A. Selloni, Phys. Rev. B: Condens. Matter 63 (2001) 155409–155418.
[26] A. Selloni, Nat. Mater. 7 (2008) 613–615.
[27] X.Q. Gong, A. Selloni, J. Phys. Chem. B 109 (2005) 19560–19562.
[28] A. Vittadini, A. Selloni, F.P. Rotzinger, M. Grätzel, Phys. Rev. Lett. 81 (1998) 2954–2957.
[29] Y.W. Jun, M.F. Casula, J.H. Sim, S.Y. Kim, J. Cheon, A.P. Alivisatos, J. Am. Chem. Soc. 125 (2003) 15981–15985.
[30] S. Kozuch, S. Shaik, J. Am. Chem. Soc. 128 (2006) 3355–3365.
[31] S. Kozuch, S. Shaik, Acc. Chem. Res. 44 (2010) 101–110.
[32] M. Boudart, Chem. Rev. 95 (1995) 661–666.
[33] S.J.M.L. Kozuch, Martin 2 (2012) 2787–2794.
[34] W.P. Kwan, B.M. Voelker, Environ. Sci. Technol. 37 (2003) 1150–1158.
[35] L.R. Martin, M.P. Easton, J.W. Foster, M.W. Hill, Atmos. Environ. 23 (1989) 563–568.
[36] C. Walling, Acc. Chem. Res. 8 (1975) 125–131.
[37] F. Haber, J.J. Weiss, Proc. R. Soc. London, Ser. A 134 (1934) 332–351.
[38] W.G. Barb, J.H. Baxendale, P. George, K.R. Hargrave, Trans. Faraday Soc. 97 (1951) 462–500.
[39] S.H. Bossman, E. Oliveros, S. Göb, S. Siegwart, E.P. Dahlen, L. Payawan, M. Straub, M. Wörner, A.M. Braun, J. Phys. Chem. A 102 (1998) 5542–5550.
[40] M.L. Kremer, Phys. Chem. Chem. Phys. 1 (1999) 3595–3605.
[41] F. Buda, B. Ensing, M. Gribnau, E.J. Baerends, Chem. Eur. J. 7 (2001) 2775–2783.
[42] C.R. Keenan, D.L. Sedlak, Environ. Sci. Technol. 42 (2008) 1262–1267.
[43] J.A. Zazo, G. Pliego, S. Blasco, J.A. Casas, J.J. Rodriguez, Ind. Eng. Chem. Res. 50 (2011) 866–870.
[44] M. Munoz, Z.M. de Pedro, J.A. Casas, J.J. Rodriguez, Appl. Catal. B: Environ. 176 (2015) 249–265.